PAPER

A bi-functional metal-free catalyst composed of dual-doped graphene and mesoporous carbon for rechargeable lithium–oxygen batteries†

Jae-Hong Kim,‡[a] Aravindaraj G. Kannan,‡[a] Hyun-Sik Woo,[a] Dae-Gun Jin,[b] Wonkeun Kim,[b] Kyounghan Ryu[b] and Dong-Won Kim*[a]

Mesoporous carbon on nitrogen and sulfur co-doped graphene nanosheets (NSGC) was synthesized and its bi-functional catalytic activity toward oxygen reduction reaction and oxygen evolution reaction was investigated. The NSGC material showed high bi-functional catalytic activity due to the synergistic effect of co-doping of sulfur and nitrogen, as well as the presence of a hierarchical porous structure. The enhanced bi-functional catalytic activity of NSGC facilitated the efficient formation and decomposition of Li_2O_2 on the air cathode. The lithium–oxygen cell assembled with the NSGC-based air cathode delivered a high initial discharge capacity of 11 431 mA h g^{-1} and exhibited good cycling stability. The hybrid structure consisting of mesoporous carbon with co-doped graphene nanosheets can be an effective strategy to improve the round-trip efficiency and cycle life of lithium–oxygen batteries.

Introduction

Rechargeable lithium–oxygen (Li–O$_2$) batteries have received great attention for use in electric vehicles and other high-energy density storage applications due to their high theoretical energy density and open cell configuration that uses oxygen as a reactant.[1,2] The successful operation of a Li–O$_2$ battery in an organic electrolyte requires the reversible formation and decomposition of insoluble Li_2O_2 on the cathode surface during the discharge and charge processes, respectively.[3] However, the large overpotential during the oxygen reduction reaction (ORR) and oxygen evolution reaction (OER), which limits the round-trip efficiency of the Li–O$_2$ battery, should be reduced to make this battery commercially viable.[4,5] In addition, the formation of insoluble Li_2O_2 during the discharge process clogs the pores of the cathode and reduces the subsequent availability of reactants reaching the catalyst surface, thereby limiting the achievable discharge capacity.[6–8] To address these problems, rational design of porous cathode architectures and effective catalysts in a stable electrolyte is critical to improve the round-trip efficiency and cycle life of Li–O$_2$ batteries.[9–12] The most widely used catalysts for the ORR are noble metals such as platinum and palladium. However, their high cost, limited supply due to finite reserves, weak durability, and detrimental environmental effects hinder commercialization.[13–15] Recently, carbon-based nanomaterials have been widely explored as either a catalyst support or a catalyst for the ORR in different electrolytes.[16,17] In particular, graphene nanosheets with their two-dimensional, sp^2-hybridized carbon structure have received great interest due to their desirable properties such as high surface area, high electronic conductivity and charge carrier mobility, high mechanical strength and chemical stability.[18–22] Furthermore, nitrogen-doped graphene nanosheets have been demonstrated as an efficient catalyst, as a metal-free alternative to Pt for the ORR because of their distinct electronic properties induced by conjugation between the lone-paired electrons of nitrogen and the graphene π system.[23] Also, N-doped graphene derives a negative charge in respect to the delocalized, sp^2-hybridized carbon framework from the lone-pair electrons of nitrogen. In addition, co-doping of graphene nanosheets with one or more additional heteroatoms (B, S, and P) is known to synergistically enhance the performance through induced structural distortions as well as modification of the charge and spin densities in the carbon structure.[24] Metal oxides such as ruthenium oxide and iridium oxide are widely used as catalysts in the OER but are not active for the ORR.[14] This has led to the search for cost-effective bi-functional catalysts that are active toward both OER and ORR. Although metal oxides such as perovskites have been recently explored as bi-functional catalysts, reports on the use of carbon-based bi-functional catalysts are very limited.[25–29] Recently, Tian *et al.* demonstrated the bi-functional catalytic activity of a nitrogen-doped graphene/carbon nanotube hybrid.[28] Zhang *et al.* prepared nitrogen and phosphorus co-

[a]Department of Chemical Engineering, Hanyang University, Seoul 133-791, Republic of Korea. E-mail: dongwonkim@hanyang.ac.kr; Fax: +82 2 2298 4101; Tel: +82 2 2220 2337

[b]Automotive Research and Development Division, Hyundai Motor Group, Gyeonggi-do 437-815, Republic of Korea

‡ J.-H. Kim and A. G. Kannan contributed equally to this work.

18456 | *J. Mater. Chem. A*, 2015, **3**, 18456–18465

This journal is © The Royal Society of Chemistry 2015

doped mesoporous nanocarbon and showed that the prepared nanocarbon can act as a bi-functional catalyst in zinc–air batteries.[27] In addition to the catalytic activity, the nature and size of the porous morphology of the air cathode might also play critical roles in determining its performance.[30] Hence, controlling the pore structures of the air cathode and employing a bi-functional electrocatalyst toward the ORR and OER are vital to further enhance the performance of Li–O_2 cells.

In this work, mesoporous carbon was grown on graphene nanosheets by *in situ* nitrogen and sulfur co-doping (hereafter referred to as NSGC) using a two-step synthesis method, as illustrated in Fig. 1. Nitrogen and sulfur were chosen due to their higher electronegativity and larger atomic size, respectively, compared to carbon atoms, which results in the modification of the structure as well as the charge and spin densities of carbon, resulting in enhanced electrocatalytic activity.[31,32] Also, the growth of mesoporous carbon on graphene nanosheets prevents the restacking of graphene, resulting in a higher active surface area and enhanced electronic conductivity.[33] Furthermore, the mesoporous structures present can accommodate the insoluble Li_2O_2 formed during discharge. As a result, the synthesized NSGC exhibited enhanced bi-functional catalytic activity toward ORR and OER, and showed a high initial discharge capacity of 11 431 mA h g^{-1} and good cycling stability as an air cathode in Li–O_2 batteries.

Experimental

Materials synthesis

Graphite oxide was prepared using a two-step modified Hummer's method from graphite powder (SP-1, 30 μm nominal particle size, Bay Carbon, USA). In the first step, pre-oxidation of graphite was carried out as reported by Kovtyukhova *et al.*[34] In the subsequent step, further oxidation was achieved using Hummer's method.[35] Graphene oxide (GO) was finally obtained by exfoliating the prepared graphite oxide using ultra-sonication. NSGC was prepared using a simple hydrothermal method, followed by a pore activation step using heat treatment at 800 °C, as previously reported.[33] In a typical synthesis procedure, 4.8 g of sucrose and 300 mg of thiourea were added to a dispersion of 200 mg of GO in 60 mL DI water and sonicated for 1 h. The mixture was further stirred for 4 h and then transferred into a Teflon-lined stainless steel autoclave and maintained at 180 °C for 12 h. The autoclave was allowed to cool naturally, and the resulting gel was alternatively washed with DI water and ethanol and then dried overnight at 120 °C in a vacuum oven. In the pore activation step, the intermediate product was mixed with potassium hydroxide at a ratio of 1 : 5 and heat-treated at 800 °C for 1 h at a heating rate of 5 °C min^{-1} in an Ar atmosphere. The resulting product was washed with a 10% hydrochloric acid solution and rinsed with DI water to neutral pH. Finally, the obtained powder was dried at 120 °C in a vacuum oven. Undoped mesoporous carbon on graphene (GC) was prepared as a control sample to investigate the effect of heteroatom doping using a similar procedure except that thiourea was not added during the hydrothermal step.

Characterization

The morphology of the prepared samples was characterized using scanning electron microscopy (SEM, JEOL JSM 6701F) and transmission electron microscopy (TEM, JEOL, JEM 2100F). X-ray photoelectron spectroscopy (XPS, VG multilab ESCA system, 220i) was used to examine the nature and amounts of dopants in the samples and to quantify the degree of GO reduction. Also, the prepared samples were characterized using Raman spectroscopy (Dongwoo Optron, MonoRa 780i) to
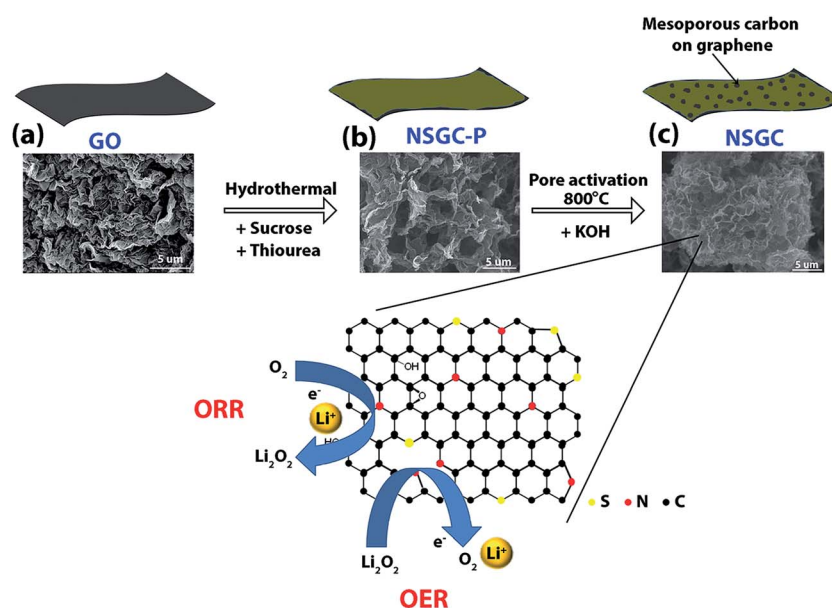

Fig. 1 Schematic illustration of the synthesis of NSGC using a two-step method (top), and the corresponding SEM images (middle). The schematic (bottom) also illustrates the metal-free bi-functional catalytic nature of NSGC toward ORR and OER.

determine their structures and investigate the graphene quality. Nitrogen adsorption/desorption isotherms were recorded using an Autosorb-IQ MP (Quantachrome INC.) apparatus at 77 K, where the samples were degassed at 100 °C for 3 h prior to measurement. X-ray diffraction (XRD) patterns were obtained using a Rigaku D/MAX 2500 diffractometer in the scan range of 10 to 40°.

Electrochemical measurements

Rotating disk electrode (RDE) measurements were carried out to investigate the electrocatalytic activities of Ketjen black (KB), GC, and NSGC toward the ORR in an organic electrolyte using a potentiostat (CH Instrument 760D) and a rotation speed controller (Pine Instrument Co. AFMSRCE). The organic electrolyte was 1 M lithium bis(trifluoromethane) sulfonylimide (LiTFSI) dissolved in tetra(ethylene glycol) dimethyl ether (TEGDME). Carbon materials (KB, GC, and NSGC) were dispersed in an ethanol solution at a concentration of 1 mg mL^{-1}, and a 10 wt% Nafion/ethanol dispersion was used to aid the adhesion of carbon particles to a glassy carbon disk electrode (diameter: 5 mm). The loading of catalyst in the RDE was 0.35 mg cm^{-2}. A Pt wire and Ag/AgCl were used as counter and reference electrodes, respectively. The air cathode was prepared by coating an *N*-methyl pyrrolidone (NMP)-based slurry containing KB/GC/NSGC as the active material, conducting carbon (KB), and poly(vinylidene fluoride) (PVDF) binder (7 : 2 : 1 by weight) on a 35BC (SGL GROUP, Germany) gas diffusion layer. The loading of active carbon materials in the air electrode was about 1.0 mg cm^{-2}. The lithium–oxygen cells composed of a lithium metal anode (Honjo Metal Co. Ltd., 200 μm thick), a glass microfiber filter separator (Whatman grade GF/C), and an air cathode were assembled with an electrolyte solution (1.0 M LiTFSI in TEGDME) into a custom-designed Swagelok-type cell fabricated from Teflon, as reported earlier.[36,37] All cells and electrolytes were prepared in an argon-filled glovebox with H$_2$O and O$_2$ contents less than 1 ppm. Galvanostatic intermittent titration technique (GITT) measurements were performed after the first discharge at a current density of 0.1 mA cm^{-2} (100 mA g$_{carbon}$$^{-1}$) for 5 h, followed by charging at the same current density for 1 h after a 12 h relaxation time. Galvanostatic cycling was performed at a constant current rate of 100 mA (g$_{carbon}$)$^{-1}$ in the voltage range of 2.5 to 4.3 V using a WBCS3000 battery cycler (WonAtech, Korea). We considered the mass of carbon materials as the active material loaded in the air electrode. For the cycling tests, the cell was placed in a chamber filled with high-purity oxygen gas at a pressure slightly above 1.0 atm.

Results and discussion

The growth of mesoporous carbon on graphene nanosheets along with simultaneous dual-heteroatom-doping *via* a simple two-step method is schematically illustrated in Fig. 1. During the hydrothermal treatment in the first step, the formation of hydrochars on the GO surface and the heteroatom doping process occur simultaneously. Here, sucrose acts as a carbon source, and thiourea acts as a source of both nitrogen and sulfur

dopants.[38] The oxygen-containing functional groups in GO and the formed hydrochars react with the decomposition products of thiourea such as ammonia and hydrogen sulfide to form C–N and C–S bonds, respectively.[39–41] The resulting hydrochar on the graphene surface (NSGC-p) is transformed into mesoporous carbon through a chemical activation step using potassium hydroxide at 800 °C. During this step, GO is simultaneously thermally reduced to form reduced graphene oxide (rGO). The SEM image of GO in Fig. 1(a) shows a crumpled sheet-like morphology, which, upon hydrothermal treatment, transforms to a sponge-like morphology with macroporous structures (Fig. 1(b)). The SEM image in Fig. 1(c) shows individual sheet-like structures that are aggregated to form a foam-like morphology upon pore activation through further heat treatment at 800 °C. The graphene/mesoporous carbon hybrid (GC) prepared as a control sample shows a similar morphology (Fig. S1 in the ESI†). The amount of GO used in the initial reaction mixture is only 4 wt%, which is enough to block the stacking of hydrochars produced in the first step. This could result in a higher surface area while maintaining the high electronic conductivity of rGO.

The morphology of the prepared NSGC was investigated using TEM analysis. The NSGC sample shows a highly folded morphology (Fig. 2(a)), which is typical for hydrothermally treated graphene-based samples. In addition, doping of larger heteroatoms such as sulfur in the carbon matrix creates a high curvature on the carbon surface, which results in highly wrinkled and curved morphologies.[42] The high-resolution TEM (HRTEM) image in Fig. 2(b) shows the presence of densely formed mesoporous structures on both sides of the graphene sheets. Fig. 2(c), (d), (e) and (f) show the TEM image and the corresponding elemental mappings of carbon, sulfur, and nitrogen, respectively. The elemental mappings of carbon, sulfur, and nitrogen atoms reveal even distributions of these atoms throughout the NSGC. This result indicates that the doped heteroatoms are uniformly present both on the basal plane and on the edges of graphene, as well as on the mesoporous carbon.

To further understand the chemical nature and bonding configuration of the doped heteroatoms, XPS analysis was carried out, and the resulting spectra are shown in Fig. 3. The XPS survey spectrum of the GC sample in Fig. 3(a) shows the presence of C 1s and O 1s peaks, whereas the spectrum of the NSGC sample shows the presence of N 1s and S 2p peaks as well as C 1s and O 1s peaks. This result confirms the successful doping of nitrogen and sulfur heteroatoms in the NSGC, which were measured to be 1.05 at% and 2.15 at%, respectively. The calculated C/O ratios in GO and NSGC were found to be 1.91 (66.2/33.8) and 12.66 (89.7/7.1), respectively. The higher C/O ratio in NSGC indicates that the oxide groups present on the GO surface and on the hydrochars are highly reduced during the pore activation step at 800 °C. The high-resolution C 1s peak of NSGC (Fig. 3(b)) was resolved into three peaks at 284.5, 285.4, and 288.8 eV. The peak at 284.5 eV indicates the presence of sp^2-hybridized carbon, and the peak at 285.9 eV confirms the presence of C–S, C–N, and C–O bonds.[43] The peak observed at 288.8 eV demonstrates the presence of residual carbonyl and

18458 | *J. Mater. Chem. A*, 2015, **3**, 18456–18465

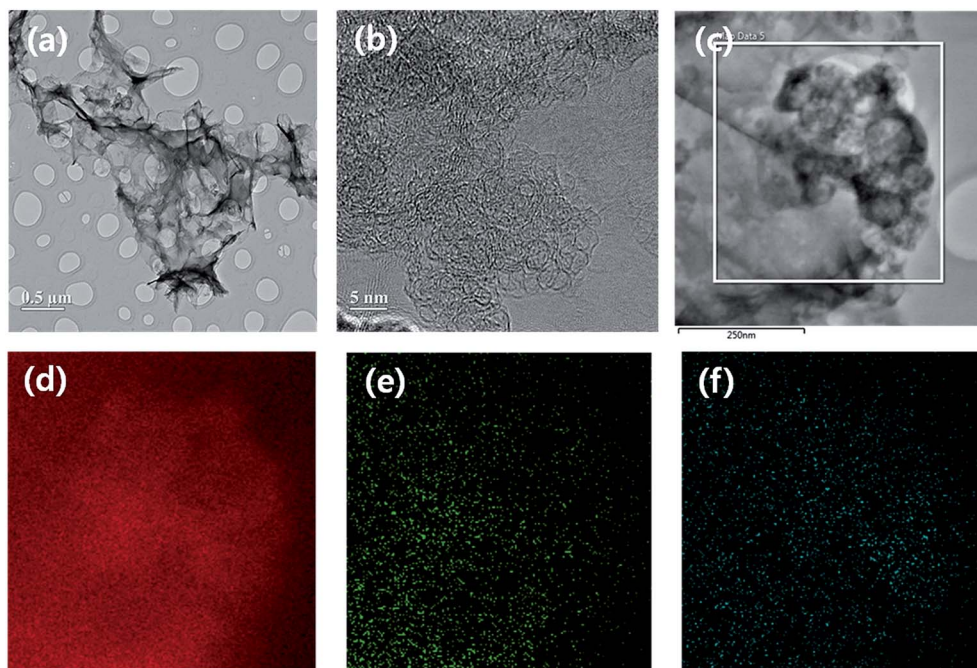This journal is © The Royal Society of Chemistry 2015

Fig. 2 (a) TEM and (b) HRTEM images of NSGC showing the mesoporous morphology on the rGO surface. Elemental mappings of NSGC: (c) TEM image, (d) C mapping, (e) S mapping, and (f) N mapping.

carboxyl groups. The S 2p peak shown in Fig. 3(c) was also resolved into three peaks. The peaks at 163.6 and 164.3 eV correspond to sulfur atoms bound in aromatic carbon structures, whereas the low intensity peak at 168.1 eV is attributed to $C-SO_x$ states.[44] The minor peak at the higher binding energy accounts for only 6.2% of the total sulfur present in the NSGC, indicating that the doped sulfur is predominantly incorporated in the carbon framework. The deconvolution of the N 1s peak (Fig. 3(d)) shows three peaks centered at 397.9, 399.5, and 401 eV, which are attributed to pyridinic-, pyrrolic-, and graphitic-type nitrogen, respectively.[45] Graphitic N is bonded to two adjacent carbon atoms, replacing a carbon atom in the carbon framework, and is present both at the edges and in the basal plane. On the other hand, pyridinic- and pyrrolic-N are present at the edges or in the defect sites present in the basal plane and are bonded to two adjacent carbon atoms.[46] These results confirm the successful doping of nitrogen and sulfur atoms in the carbon framework.

To evaluate the surface areas and pore size distributions of the prepared NSGC and GC samples, nitrogen adsorption/desorption measurements were carried out. The nitrogen adsorption/desorption isotherm of NSGC (Fig. 4(a)) shows a type IV adsorption isotherm with a steep initial region indicating the presence of micropores, followed by a sharp condensation step and a type II hysteresis loop (IUPAC classification), indicating the existence of a large number of mesopores with an average pore size of 4 nm (Fig. 4(b)). The Brunauer–Emmett–Teller (BET) surface area of NSGC was determined to be 1730 m^2 g^{-1} with a mesoporous surface area of 1032 m^2 g^{-1}. These values are significantly higher than the values reported for nitrogen and sulfur dual-heteroatom-doped

graphene nanosheets ($\sim$130 m^2 g^{-1}), indicating that mesoporous structures were successfully formed on the graphene surface. The GC sample shows similar nitrogen adsorption/desorption isotherms (ESI, Fig. S2†) with the presence of both micro- and meso-pores. The BET surface area of GC was measured to be 1658 m^2 g^{-1} with a mesoporous surface area of 928 m^2 g^{-1}. The catalytic performance of carbon-based samples is known to be influenced by the surface area of the catalyst. Since NSGC and GC show similar nitrogen adsorption/desorption isotherms, the effect of surface area on the catalytic performances of NSGC and GC could be eliminated. The Raman spectra of GO and NSGC (Fig. 4(c)) show characteristic D and G bands. The D band is centered at 1362 cm^{-1} in both GO and NSGC, which is attributed to the sp^3 distortion caused by the local plane derivatization. The G band arises from the sp^2-hybridized graphitic carbon atoms, and the G band of NSGC is more red-shifted to 1589 cm^{-1} compared to that of GO (1599 cm^{-1}). Such a red-shift is attributed to the n-type substitutional doping of graphene and thus confirms the doping of nitrogen and sulfur heteroatoms in the graphene. The intensity ratio of D to G bands (I_D/I_G) for GO and NSGC is found to be 0.97 and 1.06, respectively. This result indicates that the amount of defect sites is increased in NSGC compared to GO, which can be attributed to the presence of defective mesoporous carbon on the graphene surface. In addition, the presence of a broad 2D band at 2700 cm^{-1} indicates the mixture of single- and few-layer graphene sheets in the NSGC. The presence of well exfoliated graphene sheets was confirmed using XRD measurements (Fig. 4(d)). The diffraction pattern of graphite shows a sharp and intense peak at $\sim$26°, corresponding to an inter-layer spacing of 0.34 nm, whereas the GO sample shows an intense and

This journal is © The Royal Society of Chemistry 2015
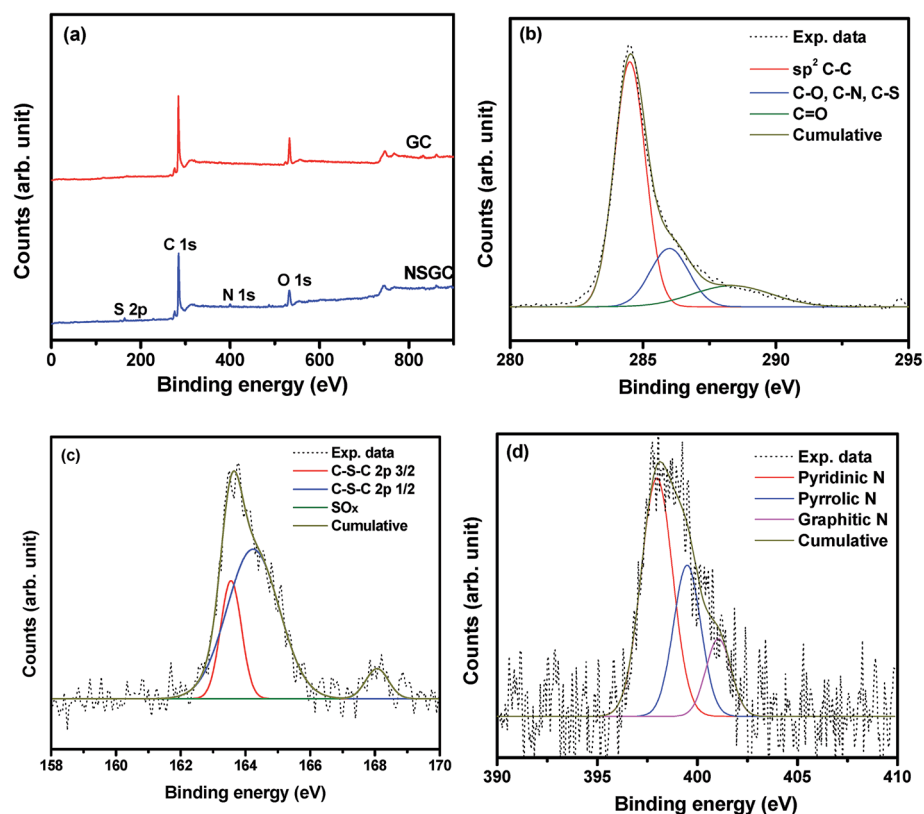
J. Mater. Chem. A, 2015, 3, 18456–18465 | 18459

Fig. 3 (a) XPS survey spectra of GC and NSGC. High-resolution XPS spectra of the NSGC sample: (b) C 1s, (c) S 2p, and (d) N 1s.

comparatively broader peak at 10.5°, corresponding to a d-layer spacing of 0.84 nm. This indicates that, upon oxidation of graphite, the oxide groups created on the individual sheets weaken the π–π interaction and can be easily exfoliated. In contrast, a very low-intensity and broad peak centered at 24.4° is observed in NSGC, suggesting that re-stacking of graphene sheets is prevented during the pore activation step mainly due to the presence of mesoporous carbon on the graphene surface.

The catalytic activities of GC and NSGC toward ORR were evaluated using RDE measurements at a rotation speed of 900 rpm in O_2-saturated 1 M LiTFSI in TEGDME at room temperature. Their performance was compared to that of KB. Here, KB was used as a control sample since it has been widely used in Li–O_2 batteries as an air cathode. Fig. 5(a) presents the voltammetric response of the samples (KB, GC, and NSGC) in the potential range of 3.0 to 2.2 V, where the current densities are normalized to the carbon loading weight. The onset potential and current density are two key indicators of catalytic activity, where a higher onset potential indicates a lower overpotential for the ORR, and a higher current density corresponds to higher catalytic activity. Also, the observed cathodic currents were directly correlated with the amount of oxygen reduced with dissolved Li^+ ions in the electrolyte to form lithium peroxide (Li_2O_2) on the surface of the carbon material in the air cathode. The ORR onset potential of NSGC was observed to be at a higher potential compared to those of the KB and GC samples. In spite of no obvious limiting current plateau in any of the samples, which is a well-known phenomenon of non-noble metal

catalysts (in particular, carbon materials), the current density of NSGC at 2.2 V (10.4 A g^{-1}) was 1.4 times higher than that of KB (7.2 A g^{-1}). Also, the current density of NSGC was higher than that of GC (9.7 A g^{-1}), indicating that NSGC exhibits superior electrocatalytic performance compared to the control samples. The higher catalytic activities of GC and NSGC compared to that of KB are attributed to their large surface areas, which can accommodate insoluble reaction products, improved electronic conductivity, and the presence of defect sites on the carbon structure. Since both NSGC and GC show similar porous morphologies and other characteristics, the better performance of NSGC could be attributed to the positive influence of heteroatom doping. The homogenous distributions of doped heteroatoms throughout NSGC, which act as catalytic centers, provide nucleation sites for the reaction products, resulting in improved performance. To further demonstrate the superior ORR electrocatalytic activity of NSGC, the power density of NSGC was calculated and compared with those of KB and GC, as shown in Fig. 5(b). The maximum power density of NSGC (26.4 W g^{-1}) was obtained at 2.0 V, which is 60% higher than that of KB (16.4 W g^{-1}) and 13% higher than that of GC (22.9 W g^{-1}). These results were supported by the faster ORR kinetics of NSGC in the electrolyte, as observed in the Tafel plot shown in Fig. 5(c). The NSGC sample exhibits the smallest slope (299 mV per decade) among the tested samples, which confirms its superior ORR kinetics in the electrolyte compared to those of GC (309 mV per decade) and KB (314 mV per decade).[47] Also, the improved OER catalytic activity of NSGC was further evaluated
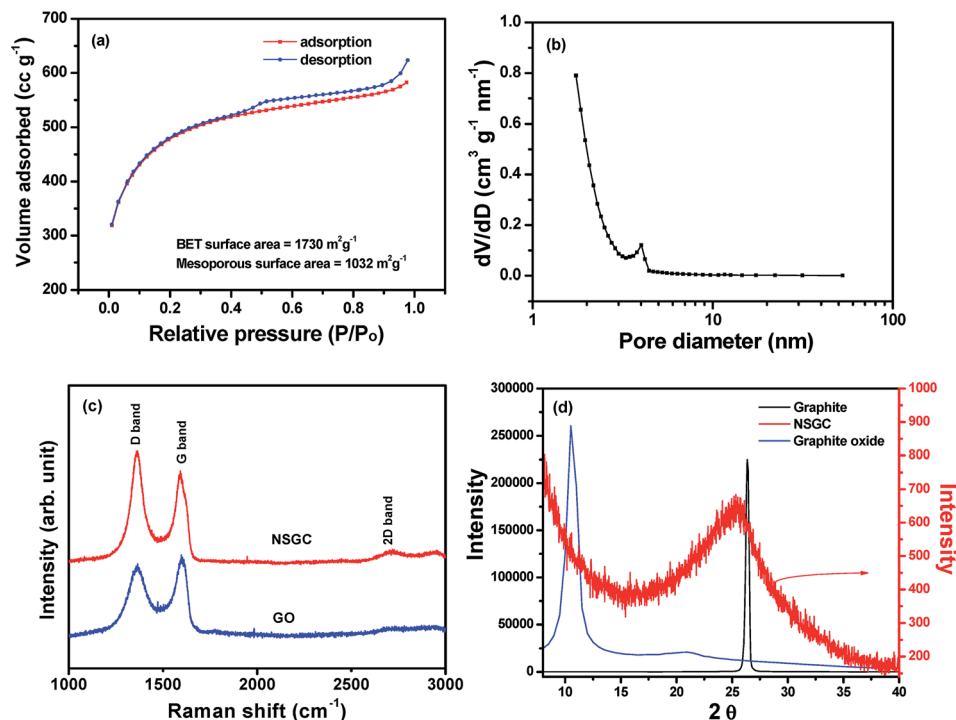
Fig. 4 (a) Nitrogen adsorption/desorption isotherm, (b) pore size distribution of NSGC, (c) Raman spectra of NSGC and GO showing the presence of G, D, and 2D bands, and (d) XRD patterns of graphite, graphite oxide and NSGC.

using GITT and the results are shown in Fig. 5(d). GITT is an electrochemical technique that combines transient and steady-state processes, and can be utilized to determine the over-potential of the electrochemical system.[48,49] The NSGC sample shows a lower overpotential during charging in each interval compared to the control samples, indicating the superior OER catalytic activity of NSGC. The improved bi-functional electro-catalytic activity of NSGC is attributed to the following factors: (a) the synergistic effect of co-doping of nitrogen and sulfur heteroatoms on carbon nanostructures to alter the charge and spin densities of carbon; (b) the presence of mesoporous carbon on graphene nanosheets that complement each other, in which graphene nanosheets enhance the electronic conductivity, while mesoporous carbon provides a larger accessible surface area and prevents restacking of graphene nanosheets; (c) the uniform distribution of doped heteroatoms throughout the sample, which act as catalytic centers, resulting in numerous nucleation sites for the growth of reaction products, which reduces the size of the product formed; (d) the presence of hierarchical porous structures that can accommodate the insoluble reaction product formed during the discharge step and allow an easy pathway for ion movement.

The electrochemical performances of NSGC and the other control samples as an air cathode in a Li–O$_2$ cell were evaluated using a Swagelok-type cell, and the full charge–discharge capacities of Li–O$_2$ cells were determined at a constant current density of 0.1 mA cm^{-2} (100 mA g$_{carbon}$$^{-1}$). Fig. 6(a) shows the first discharge–charge curves of the cells assembled with the different electrodes. The cell with the NSGC-based air cathode exhibited the highest capacity and efficiency among the tested

carbon materials. These results confirm the excellent perfor-mance of the NSGC-based air cathode in an organic electrolyte because of its enhanced catalytic effect toward OER and ORR compared to those of other carbon materials. Moreover, the large accessible surface areas of the NSGC and GC samples can accommodate the insoluble oxygen reduction product (Li$_2$O$_2$) during the discharge step. Also, as shown in Fig. 6(b), the NSGC-based cell exhibits not only a higher discharge capacity, but also a lower overpotential than the KB-based cell, indicating a superior catalytic effect for an air cathode in Li–O$_2$ cells without any metallic catalysts.

In order to evaluate the reversibility of the NSGC-based air cathode in Li–O$_2$ cells, SEM and XRD analyses were carried out in the pristine state, after discharge, and after recharge states. The SEM image of the NSGC-based air cathode before cycling, shown in Fig. 7(a), exhibits a macroporous morphology with a sponge-like sheet shape of NSGC, whereas the NSGC-based air cathode after the fifth discharge is deposited with ORR products on the surface of the NSGC (Fig. 7(b)). These particles are believed to be Li$_2$O$_2$, which is associated with the product from the ORR and is no longer present on the NSGC surface after recharging (Fig. 7(c)). The air cathode after cell recharging has a very similar morphology to that of the pristine electrode with sharp-edged particles. The reversibility of the Li–O$_2$ cell with the NSGC-based air cathode was further confirmed by XRD analysis. Fig. 7(d) shows the XRD patterns of the NSGC-based air cathode as a function of the state of charge. The XRD pattern obtained after discharge shows the characteristic crystalline peaks cor-responding to Li$_2$O$_2$. This result suggests that the NSGC-based electrode can play a role as a desired ORR catalyst. After

This journal is © The Royal Society of Chemistry 2015
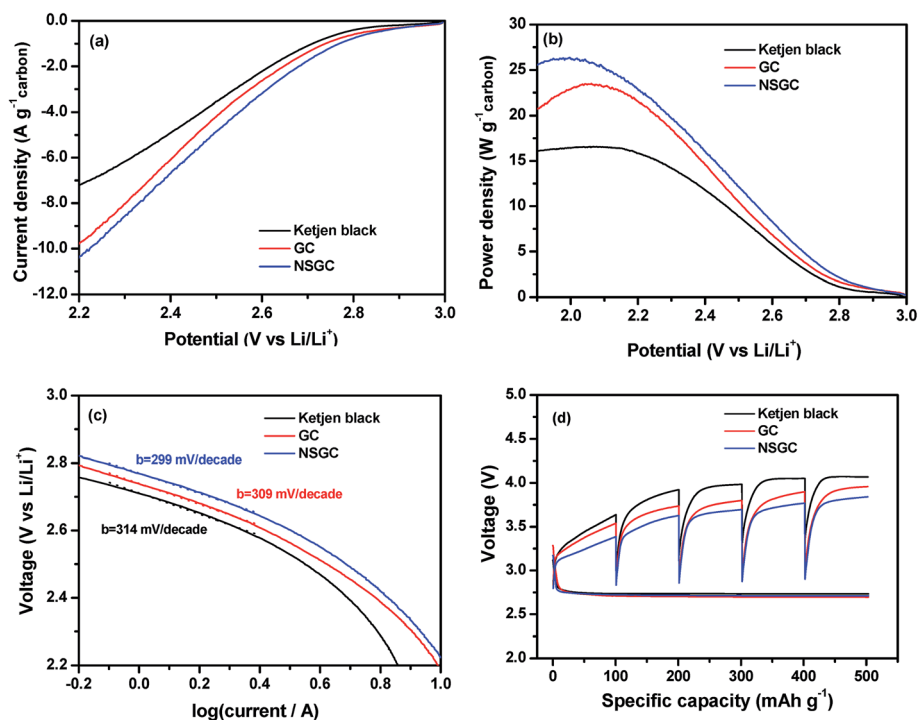
J. Mater. Chem. A, 2015, 3, 18456–18465 | 18461

Fig. 5 (a) ORR polarization curves of Ketjen black, GC and NSGC in the O_2-saturated electrolyte (1 M LiTFSI in TEGDME) at a scan rate of 5 mV s^{-1} and a rotation rate of 900 rpm, (b) power density, (c) Tafel plots of Ketjen black, GC and NSGC, and (d) GITT curves of the Li–O_2 batteries with Ketjen black, GC and NSGC-based air cathodes.
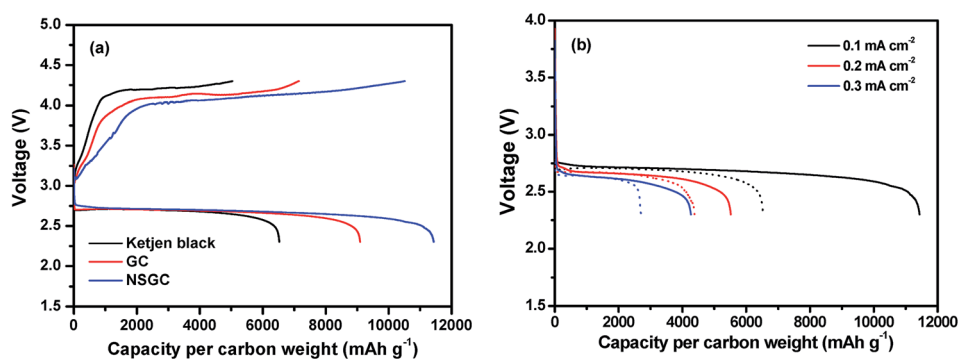

Fig. 6 (a) Initial discharge and charge curves of lithium–oxygen cells assembled with different electrode materials obtained between 2.3 and 4.3 V at a constant current density of 0.1 mA cm^{-2} (100 mA g^{-1}), and (b) initial discharge curves of the lithium–oxygen cells with KB (dotted line) and NSGC (solid line) at different current densities.

recharging, no characteristic Li_2O_2 peaks were present in the XRD pattern, confirming the decomposition of Li_2O_2 *via* the OER.

Fig. 8 shows the charge and discharge curves of the lithium–air cells assembled with the different electrode materials, measured with a capacity cut-off of 1000 mA h g^{-1}. The overpotential of the NSGC-based electrode is lower than those of the other electrodes because of its faster kinetics in the OER and ORR. In the NSGC-based Li–O_2 cell, reversible charge and discharge cycling was observed up to the 38th cycle, which is more stable than the cells with KB or GC. In order to achieve improved cycling performance of the Li–O_2 cells, the depth of discharge was reduced from 1000 to 500 mA h g^{-1} (Fig. 9). When

the specific capacity is limited to 500 mA h g^{-1}, the amount of ORR products formed on the carbon surface is reduced, which inhibits the pore clogging of the air cathode and suppresses polarization of the electrode. Therefore, the cycle performance of the Li–O_2 cell assembled with the NSGC-based air cathode was remarkably improved over 100 cycles without any significant voltage profile change. The cycling results shown in Fig. 8 and 9 demonstrate that the cycling stability of the lithium–air cell with the NSGC-based air cathode is much better than those of the cells with other carbon materials (KB and GC). More systematic studies on the optimization of the air cathode, such as the amount of doping and types of binders and electrolytes, are currently in progress to accomplish improved cycling
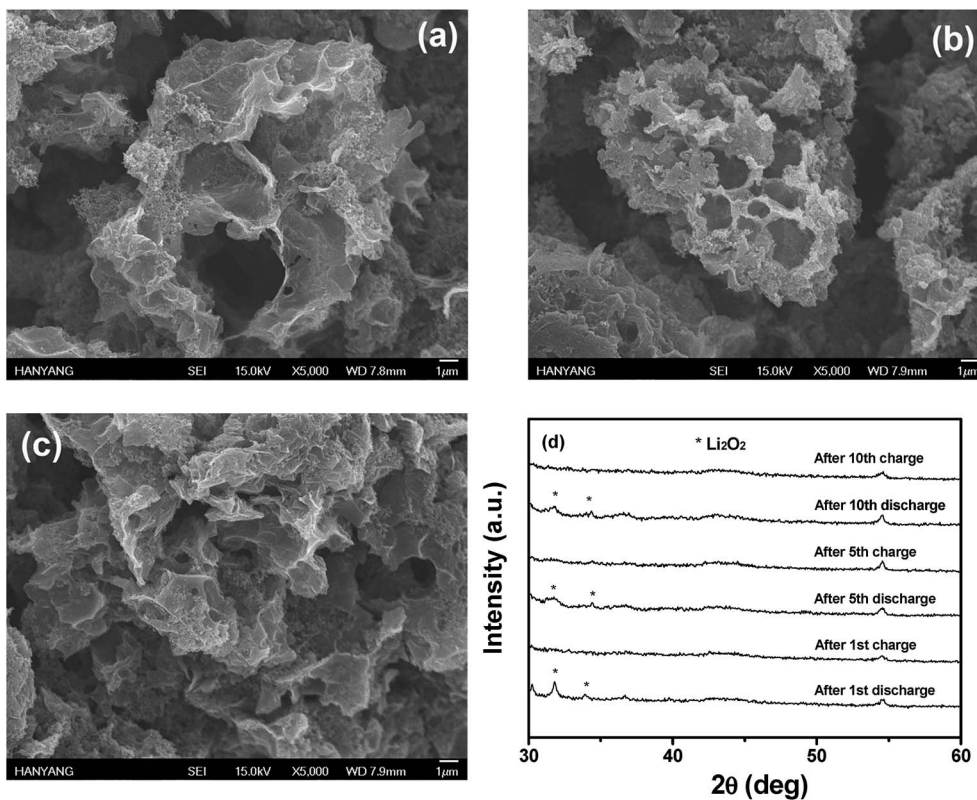
Fig. 7   SEM images of the NSGC-based electrode (a) before cycling, (b) after the fifth discharge cycle, and (c) after the fifth charge cycle. (d) XRD diffraction patterns of the NSGC-based electrode analyzed at different charge states.
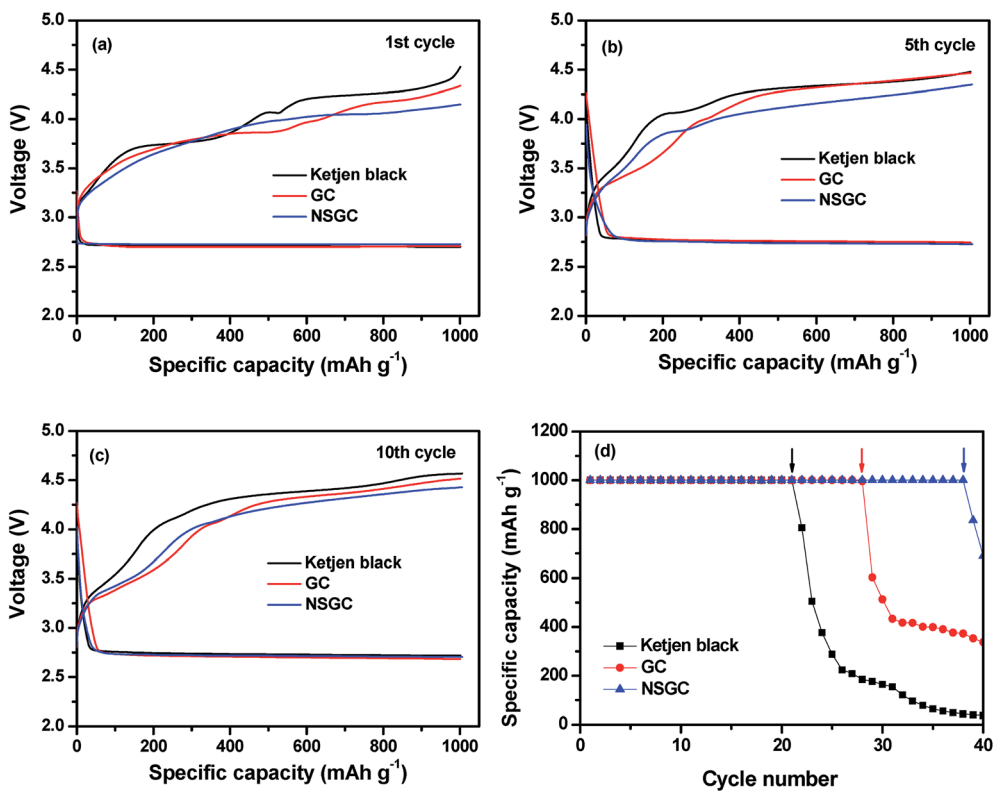

Fig. 8   Charge and discharge voltage profiles of the Ketjen black, GC and NSGC electrodes at the (a) first, (b) fifth, and (c) 10th cycles. (d) Specific discharge capacities of the lithium−O_2 cells assembled with different electrode materials as a function of cycle number (100 mA g^{-1}, 10 h cut-off).
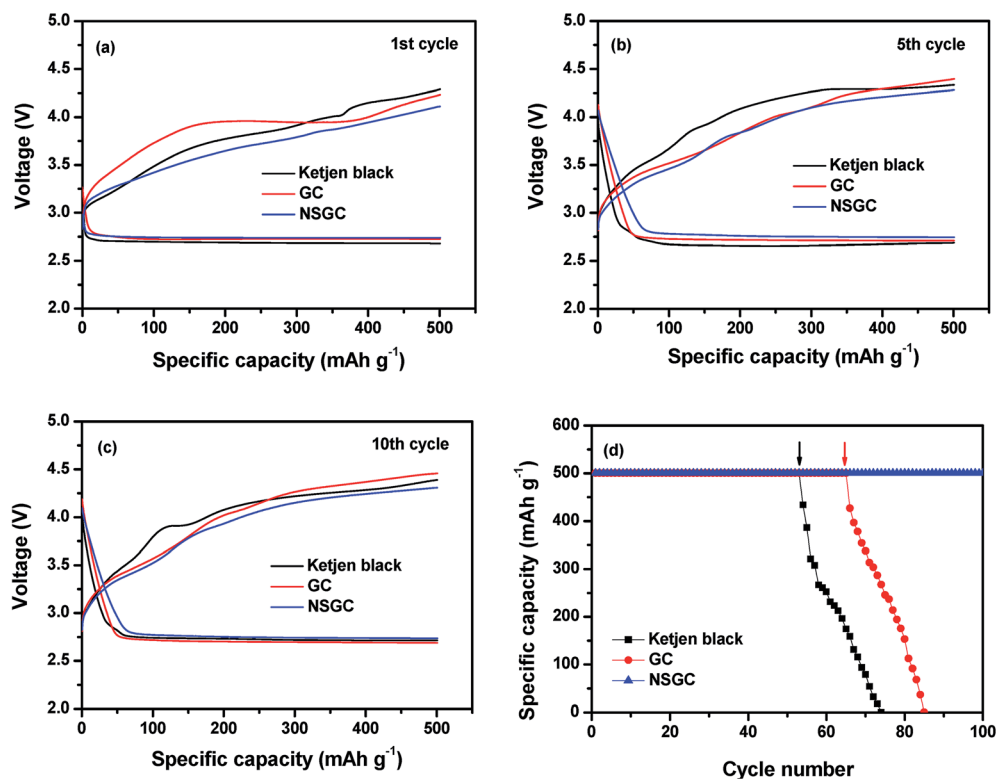
Fig. 9 Charge and discharge voltage profiles of the Ketjen black, GC and NSGC electrodes at the (a) first, (b) fifth, and (c) 10th cycles. (d) Specific discharge capacities of the lithium−O_2 cells assembled with different electrode materials as a function of cycle number (50 mA g^{-1}, 5 h cut-off).

performance of lithium–oxygen cells with the NSGC-based air cathode.

Conclusions

We demonstrated that the growth of mesoporous carbon on graphene nanosheets along with nitrogen and sulfur hetero-atom co-doping can effectively act as a metal-free bi-functional catalyst toward ORR and OER. The enhanced bi-functional catalytic activity of NSGC in comparison to the undoped gra-phene and KB samples facilitates more efficient formation and decomposition of Li_2O_2 during discharge and charge cycling, respectively. The NSGC air cathode showed higher initial capacities and an improved rate capability. The enhanced performance of the NSGC sample is attributed to the synergistic effects of co-doping of sulfur and nitrogen heteroatoms and the presence of hierarchical porous structures, which can accom-modate the insoluble discharge products. Thus, it is suggested that co-doping of a graphene/mesoporous carbon hybrid along with control of the porous morphology is an effective strategy to improve the round-trip efficiency and cycle life of Li–O_2 cells.

Acknowledgements

References

1 P. G. Bruce, S. A. Freunberger, L. J. Hardwick and J.-M. Tarascon, *Nat. Mater.*, 2012, **11**, 19–29.

2 L. Grande, E. Paillard, J. Hassoun, J.-B. Park, Y.-J. Lee, Y.-K. Sun, S. Passerini and B. Scrosati, *Adv. Mater.*, 2015, **27**, 784–800.

3 S. Kang, Y. Mo, S. P. Ong and G. Ceder, *Chem. Mater.*, 2013, **25**, 3328–3336.

4 R. Black, B. Adams and L. F. Nazar, *Adv. Energy Mater.*, 2012, **2**, 801–815.

5 F. Li, T. Zhang and H. Zhou, *Energy Environ. Sci.*, 2013, **6**, 1125–1141.

6 H.-D. Lim, H. Song, H. Gwon, K.-Y. Park, J. Kim, Y. Bae, H. Kim, S.-K. Jung, T. Kim, Y. H. Kim, X. Lepro, R. Ovalle-Robles, R. H. Baughman and K. Kang, *Energy Environ. Sci.*, 2013, **6**, 3570–3575.

7 X. Lin, L. Zhou, T. Huang and A. Yu, *J. Mater. Chem. A*, 2013, **1**, 1239–1245.

8 J. Xiao, D. Mei, X. Li, W. Xu, D. Wang, G. L. Graff, W. D. Bennett, Z. Nie, L. V. Saraf, I. A. Aksay, J. Liu and J.-G. Zhang, *Nano Lett.*, 2011, **11**, 5071–5078.

9 F. Cheng and J. Chen, *Chem. Soc. Rev.*, 2012, **41**, 2172–2192.

10 J. Lu, L. Li, J.-B. Park, Y.-K. Sun, F. Wu and K. Amine, *Chem. Rev.*, 2014, **114**, 5611–5640.

18464 | *J. Mater. Chem. A*, 2015, **3**, 18456–18465

This journal is © The Royal Society of Chemistry 2015

11 L. Li, S.-H. Chai, S. Dai and A. Manthiram, *Energy Environ. Sci.*, 2014, **7**, 2630–2636.

12 A. Manthiram and L. Li, *Adv. Energy Mater.*, 2015, **5**, DOI: 10.1002/aenm.201401302.

13 R. Cao, J.-S. Lee, M. Liu and J. Cho, *Adv. Energy Mater.*, 2012, **2**, 816–829.

14 Z.-L. Wang, D. Xu, J.-J. Xu and X.-B. Zhang, *Chem. Soc. Rev.*, 2014, **43**, 7746–7786.

15 Y.-C. Lu, H. A. Gasteiger and Y. Shao-Horn, *J. Am. Chem. Soc.*, 2011, **133**, 19048–19051.

16 C. Zhu and S. Dong, *Nanoscale*, 2013, **5**, 1753–1767.

17 N. Daems, X. Sheng, I. F. J. Vankelecom and P. P. Pescarmona, *J. Mater. Chem. A*, 2014, **2**, 4085–4110.

18 A. K. Geim and K. S. Novoselov, *Nat. Mater.*, 2007, **6**, 183–191.

19 A. K. Geim, *Science*, 2009, **324**, 1530–1534.

20 D. Geng, N. Ding, T. S. Andy Hor, Z. Liu, X. Sun and Y. Zong, *J. Mater. Chem. A*, 2015, **3**, 1795–1810.

21 H. Kim, H.-D. Lim, J. Kim and K. Kang, *J. Mater. Chem. A*, 2013, **2**, 33–47.

22 C. Huang, C. Li and G. Shi, *Energy Environ. Sci.*, 2012, **5**, 8848–8868.

23 L. Lai, J. R. Potts, D. Zhan, L. Wang, C. K. Poh, C. Tang, H. Gong, Z. Shen, J. Lin and R. S. Ruoff, *Energy Environ. Sci.*, 2012, **5**, 7936–7942.

24 J. P. Paraknowitsch and A. Thomas, *Energy Environ. Sci.*, 2013, **6**, 2839–2855.

25 J.-J. Xu, D. Xu, Z.-L. Wang, H.-G. Wang, L.-L. Zhang and X.-B. Zhang, *Angew. Chem., Int. Ed.*, 2013, **52**, 3887–3890.

26 Y. Zhao, L. Xu, L. Mai, C. Han, Q. An, X. Xu, X. Liu and Q. Zhang, *Proc. Natl. Acad. Sci. U. S. A.*, 2012, **109**, 19569–19574.

27 J. Zhang, Z. Zhao, Z. Xia and L. Dai, *Nat. Nanotechnol.*, 2015, **10**, 444–452.

28 G.-L. Tian, M.-Q. Zhao, D. Yu, X.-Y. Kong, J.-Q. Huang, Q. Zhang and F. Wei, *Small*, 2014, **10**, 2251–2259.

29 R. Li, Z. Wei and X. Gou, *ACS Catal.*, 2015, **5**, 4133–4142.

30 Z.-L. Wang, D. Xu, J.-J. Xu, L.-L. Zhang and X.-B. Zhang, *Adv. Funct. Mater.*, 2012, **22**, 3699–3705.

31 J. Liang, Y. Jiao, M. Jaroniec and S. Z. Qiao, *Angew. Chem., Int. Ed.*, 2012, **51**, 11496–11500.

32 Z. Liu, H. Nie, Z. Yang, J. Zhang, Z. Jin, Y. Lu, Z. Xiao and S. Huang, *Nanoscale*, 2013, **5**, 3283–3288.

33 L. Zhang, F. Zhang, X. Yang, G. Long, Y. Wu, T. Zhang, K. Leng, Y. Huang, Y. Ma, A. Yu and Y. Chen, *Sci. Rep.*, 2013, **3**, 1408.

34 N. I. Kovtyukhova, P. J. Ollivier, B. R. Martin, T. E. Mallouk, S. A. Chizhik, E. V. Buzaneva and A. D. Gorchinskiy, *Chem. Mater.*, 1999, **11**, 771–778.

35 W. S. Hummers and R. E. Offeman, *J. Am. Chem. Soc.*, 1958, **80**, 1339.

36 S.-M. Han, J.-H. Kim and D.-W. Kim, *J. Electrochem. Soc.*, 2014, **161**, A856–A862.

37 S.-M. Han, J.-H. Kim and D.-W. Kim, *J. Electrochem. Soc.*, 2015, **162**, A3103–A3109.

38 A. G. Kannan, J. Zhao, S. G. Jo, Y. S. Kang and D.-W. Kim, *J. Mater. Chem. A*, 2014, **2**, 12232–12239.

39 S. Wang, Q. Gao and J. Wang, *J. Phys. Chem. B*, 2005, **109**, 17281–17289.

40 X. Wang, X. Li, L. Zhang, Y. Yoon, P. K. Weber, H. Wang, J. Guo and H. Dai, *Science*, 2009, **324**, 768–771.

41 S. Yang, L. Zhi, K. Tang, X. Feng, J. Maier and K. Müllen, *Adv. Funct. Mater.*, 2012, **22**, 3634–3640.

42 C. H. Choi, M. W. Chung, S. H. Park and S. I. Woo, *Phys. Chem. Chem. Phys.*, 2013, **15**, 1802–1805.

43 Y. Dong, H. Pang, H. B. Yang, C. Guo, J. Shao, Y. Chi, C. M. Li and T. Yu, *Angew. Chem., Int. Ed.*, 2013, **52**, 7800–7804.

44 Z. Yang, Z. Yao, G. Li, G. Fang, H. Nie, Z. Liu, X. Zhou, X. A. Chen and S. Huang, *ACS Nano*, 2011, **6**, 205–211.

45 S.-A. Wohlgemuth, F. Vilela, M.-M. Titirici and M. Antonietti, *Green Chem.*, 2012, **14**, 741–749.

46 H. Wang, T. Maiyalagan and X. Wang, *ACS Catal.*, 2012, **2**, 781–794.

47 V. Viswanathan, J. K. Nørskov, A. Speidel, R. Scheffler, S. Gowda and A. C. Luntz, *J. Phys. Chem. Lett.*, 2013, **4**, 556–560.

48 Z. H. Cui, X. X. Guo and H. Li, *Energy Environ. Sci.*, 2015, **8**, 182–187.

49 B. G. Kim, H. J. Kim, S. Back, K. W. Nam, Y. Jung, Y. K. Han and J. W. Choi, *Sci. Rep.*, 2014, **4**, 4225.

This journal is © The Royal Society of Chemistry 2015

J. Mater. Chem. A, 2015, **3**, 18456–18465 | **18465**